Iron substitution in $Na_4VMn(PO_4)_3$ as a strategy for improving the electrochemical performance of sodium-ion batteries

P. Lavela *, R. Klee, M.A. Hidalgo, J.L. Tirado

Departamento de Química Inorgánica e Ingeniería Química, Instituto Universitario de Química Fina y Nanoquímica, Universidad de Córdoba Edificio Marie Curie. Campus de Rabanales, 14071 Córdoba, Spain

ARTICLE INFO

ABSTRACT

Six NASICON type samples with $Na_{4-x}VFe_xMn_{1-x}(PO_4)_3$ ($0 \leq x \leq 1$) stoichiometry are examined as positive electrodes for sodium-ion batteries. The structural, morphological, and chemical state of elements in raw samples is unveiled by XRD diffraction, electron microscopy, and Raman and XPS spectroscopies. The effect of the dual Fe/Mn substitution is examined by electrochemical tests using both voltammetric and galvanostatic methods. The results reveal the beneficial effect of the iron substitution, justified by an improvement of the kinetic response, and supported by the calculation of the apparent diffusion coefficients and internal cell resistance.

1. Introduction

Electrochemical sodium-ion storage is attracting more attention as a serious competitor of lithium-ion batteries. In the beginning, numerous objections were raised about the intrinsic larger ion size and lower output voltage of sodium than lithium. However, crucial benefits as the high crust and ocean abundance, the homogeneous distribution of resources, and environmental benignity of sodium have been pointed out as essential aspects to be considered in the case of limited lithium resource supply [1–6]. Moreover, the less polarizing character of sodium is expected to notably affect the phase behavior and diffusion properties. The desolvation energy for these alkaline ions has been reported to be is roughly 30% smaller than for lithium in several organic solvents, diminishing accordingly the charge transfer resistance and enhancing the electrode kinetics [7,8]. Therefore, sodium-ion batteries are nowadays envisaged for their applicability as large-scale stationary batteries supporting energy storage from renewable resources [9,10].

Sodium-ion batteries are based on the same electrochemical principles as lithium analogs, allowing rapid technological growth. Most of this advance can be attributed to the achievements of electrode materials capable to provide a fast and stable diffusion path to the large sodium ions. Despite this fact, the formation of intermediate phases during sodium insertion results in a more complex behavior needing careful attention [7]. Concerning cathode materials, research on layered oxides, polyanionic compounds and Prussian analogues have evidenced the possibility of reaching competing high output voltage, large capacity, and cycling stability [11–15].

Particularly, polyanionic compounds with $Na_3M_2(PO_4)_3$ (M = V, Fe, Mn, etc.) stoichiometry, featuring a NASICON (NAtrium SuperIonic CONductor) structure, offer a rigid and open framework able to resist the reversible insertion of large Na^+ ions for a large number of cycles. This structure can be more easily depicted as a built-up of repeating units consisting of two MO_6 octahedron sharing corners with three PO_4 tetrahedrons with a nominal $M_2(PO_4)_3$ stoichiometry. They are mutually enchained to form infinite ribbons along the c axis, creating distorted octahedral sites to host one sodium per formula unit. The extraction of this sodium is feasible but unfortunately, provokes irreversible changes in the structure affecting negatively further cycling. In addition, three large interconnected eight-fold sites (Na2) are located between these ribbons, constituting an effectve diffusion path for the remaining two Na^+ [16–19].

Among the possible compositions, much attention has been paid to vanadium-containing cathode materials because of their high output voltages and maximal attaining capacities. The multivalent character of this transition element (V^{2+} to V^{5+}), along with the low cost and relative abundancy make of V-based materials promising electrode for sodium-ion batteries [20]. Unfortunately, a large-scale application is restricted by certain vanadium toxicity. Thus, researchers are now focusing on the partial replacement of V by other environment-friendly transition metals [21–24]. Particularly, iron and manganese are abundant rock-forming elements, widely distributed in the Earth's crust, composing a large variety of proved electrode materials for sodium-

---

ion batteries [25–27]. Recently, Zhou et al. described the electrochemical behavior of $Na_4MnV(PO_4)_3$ and $Na_3FeV(PO_4)_3$, demonstrating their reliability as cathode materials for sodium-ion batteries [28].

In this work, we aim to evaluate the effect of the replacement of vanadium by different Fe/Mn ratios in the $Na_{4-x}VFe_xMn_{1-x}(PO_4)_3$ ($0 \leq x \leq 1$) series as cathode materials for sodium-ion batteries. A citric-based sol–gel route was used to prepare in-situ carbon-containing samples ensuring a proper electric conductivity. The structural and morphological properties of the raw materials have been characterized by X-ray diffraction, electron microscopy, Raman, and X-ray photoelectron spectroscopy, while galvanostatic and voltammetric techniques were helpful to examine their electrochemical behavior at different kinetic conditions.

2. Materials and methods

2.1. Material synthesis

An easy, low-cost, and scalable sol–gel procedure was employed to prepare samples of the $Na_{4-x}VFe_xMn_{1-x}(PO_4)_3$ nominal stoichiometry. Six products with × values of 0.0, 0.2, 0.4, 0.6, 0.8, and 1.0 were obtained. For this purpose, stoichiometric amounts of NH_4VO_3 (Sigma-Aldrich, $\geq$ 99%), $Fe(NO_3)_3 \cdot 9H_2O$ (Sigma-Aldrich, 99%) Mn $(CH_3COO)_2 \cdot 4H_2O$ (Aldrich, $\geq$ 99%), $NaCH_3COO$ (Aldrich, $\geq$ 99%) and NaH_2PO_4 (Aldrich, 98–102%) were used as follows. First, the transition metal salts and sodium acetate were sequentially dissolved in 50 mL of citric acid (Sigma-Aldrich, 99%) solution. The amount of the latter acid was that ensuring 3 to 1 citric to metal ratio. Next, sodium acetate was dissolved not only to provide the eventual sodium stoichiometry but also in slight excess to counterbalance losses upon calcination. Then, 50 mL of the NaH_2PO_4 solution were slowly poured from a funnel and stirred for at least one hour to ensure metal chelation. After removing the solvent in a rotor evaporator (200 mbar,

70 °C), the precursors were dried overnight at 120 °C, ball-milled and annealed in argon atmosphere following two sequential thermal plateaus at 350 °C for 4 h and 750 °C for 8 h (heating ramp of 5 °C min^{-1}). The calcined black coloured powdered product evidences the presence of a carbon conductive phase arising from the thermal decomposition of citrate in the anaerobic condition existing during the annealing process.

2.2. Material characterization

The crystalline phosphate samples were analysed by X-ray powder diffractometry (XRD) to evaluate the purity of phases with a *BrukerD8 Discover A25* diffractometer, equipped with Cu Kα radiation, Ge monochromator, and Lynxeye detector. The patterns of raw samples were scanned between 2 and 90° (2θ) (step size: 0.04° and 672 s per step). *Ex-situ* X-ray patterns of electrodes charged – discharged at C/10 along the first cycle were scanned between 20 and 60° (2θ) (step size of 0.04° and 3840 s per step). To preserve them from the air, they were covered with *Kapton* tape. The unit cell parameters were calculated by using *TOPAS v.4.2* software. The carbon content was determined by elemental *CHNS* analysis in a *Eurovector EA 3000* equipment, while the level of graphitization was calculated by recording the Raman spectra in a Renishaw Raman spectrometer furnished with a green laser light excitation source (532 nm). The morphological study of the powdered samples was performed by transmission electron microscopy (TEM) by using a JEOL 1400 microscope, and field emission scanning electron microscopy (FESEM), recorded in A JSM-7800F Prime microscope, furnished with an EDX analyzer. Elemental analysis was also determined by X-ray fluorescence (XRF) in a sequential wavelength dispersive spectrometer (ZSX Primus IV de Rigaku). The chemical state of the elements of pristine and tested electrodes was elucidated by X-ray photoelectron spectroscopy (XPS) by using a *SPECS Phobios 150 MCD* spectrometer furnished with an AlKα source.
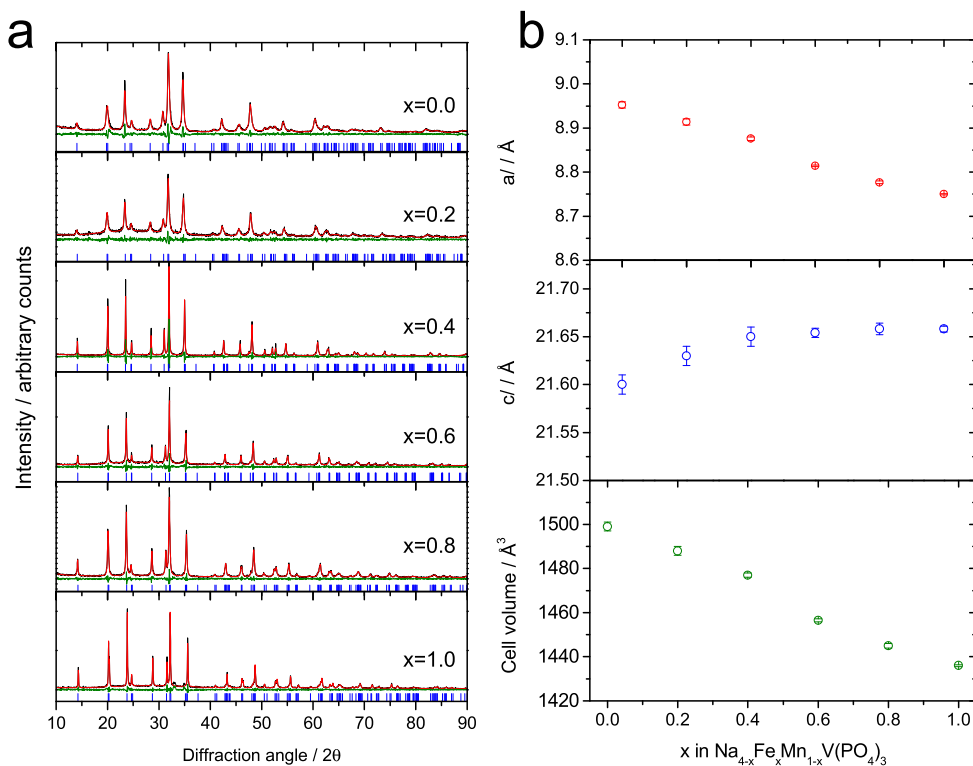

Fig. 1. a) X-ray diffraction patterns of $Na_{4-x}VFe_xMn_{1-x}(PO_4)_3$ ($0 \leq x \leq 1$) samples. Experimental patterns (black), calculated patterns (red), and differential curves (green). DIF patterns for the indexation in the *R*-3*c* space group are shown in blue color. b) Cell parameters variation as a function of the iron content. (For interpretation of the references to color in this figure legend, the reader is referred to the web version of this article.)

Appropriate measurement required, samples pelletization and out-gassing to high vacuum overnight. Binding energies were calibrated by assigning the position of the adventitious carbon C1s line to 284.6 eV.

2.3. Electrochemical characterization

Electrochemical tests were performed by assembling the raw materials as working electrodes in Swagelok™ type two-electrode cells. For this purpose, the studied compound, carbon black and polyvinylidene fluoride (PVDF) were blended in a mass ratio 7:2:1. This mixture was dispersed in *N*-methyl-2-pyrrolidone (NMP) and stirred for at least one hour to achieve a homogenous paste. The eventual electrode was prepared by spreading this paste onto a 9 mm diameter aluminium disk and dried at 120 °C in a vacuum overnight. The counter electrode was a 9 mm diameter disk of metallic sodium. The electrolyte was a 1 M NaClO$_4$:PC (propylene carbonate) solution including 2% of FEC (fluoroethylene carbonate). This solution was soaked in fiberglass (*GF/A-Whatman*) separator disks. These elements were stacked into the Swagelok™ cell and hermetically sealed in an argon-containing glovebox able to control O$_2$ and H$_2$O traces.

The electrochemical cells were subjected to voltammetric and galvanostatic cycling by using Biologic multichannel systems. Cyclic voltammetry (CV) was conducted in the potential window between 1.8 and 3.9 V vs Na$^+$/Na at scanning rates between 0.1 and 1 mV s^{-1}. Galvanostatic cycling was executed within the same potential window at C rates varying from C/10 to 5C. For the long cycling experiments at 1C, three initial activation cycles were performed at C/10. *Post-mortem* analysis was carried out on electrodes tested at C/10. Electrochemical Impedance Spectroscopy (EIS) was performed in an *SP-150 Biologic* instrument at the selected depth of charge and discharge during the first cycle at C/10 and after nine additional cycles at 1C. Before measuring, the cell was allowed to relax for 6 h to reach a quasi-equilibrium state. These spectra were recorded by perturbing the open circuit voltage with an AC signal of 5 mV from 100 kHz to 2 mHz.

3. Results and discussion

The XRD patterns in Fig. 1a revealed highly crystalline and mostly pure samples. The narrow reflections were suitably indexed in the *R-3c* space group of the trigonal system. Only minor impurities ascribable to maricite NaFePO$_4$ are observed for the sample with x = 1.0. Mortemard et al. reported this same impurity for the Na$_{3+x}$V$_{2-x}$Fe$_x$(PO$_4$)$_3$ series in samples with x ≥ 0.5 [29]. The cell parameters were calculated and displayed in Fig. 1b. On increasing the × value, an anisotropic cell contraction resulted from the progressive decrease of the parameter *a*, while *c* increases. This is a commonly observed effect in NASICON compounds in which the transition metal is partially replaced [30,31]. The cell volume decrease agrees well with the continuous replacement of larger Mn^{2+} (0.97 Å) by Fe^{3+} (0.785 Å). Zhou et al. reported a slight structural variation in Na$_3$FeV(PO$_4$)$_3$ arising from a cooperative distortion of the FeO$_6$ octahedra leading to a monoclinic crystal structure [28]. Despite this fact, we have indexed all samples in the same *R-3c* space group for comparative purposes. In addition, a peak widening is also observed when the manganese content is increased. This effect could be correlated to hindrances to crystal growth and/or crystal strains when V^{3+} (0.78 Å) is replaced by larger Mn^{2+} (0.97 Å) along with the necessity for incorporating additional Na$^+$ cations to balance the diminution of charge. Otherwise, the close similarity of V^{3+} crystal radius as compared to that of Fe^{3+} (0.785 Å) would involve minor structural variations.

The disordered character of the carbon conductive phase, obtained after annealing at 750 °C, prevented the appearance of observable XRD reflection in Fig. 1a. The broadened and low intense diffraction reflections are undoubtedly masked by the intense peaks of the highly crystalline NASICON phase. To gather some structural information on this amorphous component, Raman spectra were recorded between 1000 and 2000 cm^{-1} to at least determine the graphitization index. The spectra in Fig. 2 feature two broad and overlapped bands ascribable to disordered domains (D1 band) at 1351 ± 3 cm^{-1} and in-plane displacement of carbon atoms in the crystalline graphene sheets 1591 ± 3 cm^{-1} (G band) (Fig. 2 and Table S1) [32]. The graphitization index is defined as the ratio between the integrated area of both signals. A proper quantification of them requires a precise deconvolution of the overall profile in gaussian–lorentzian components. Sadezky et al. reported that this mathematical treatment requires the introduction of additional small components at 1500 ± 2 cm^{-1} (D3), 1167 ± 2 cm^{-1} (D4), and 1687 ± 1 cm^{-1} (D2), belonging also to amorphous carbon. [33]. The graphitization index took low values between 0.46 and 0.49 (Table S1), which is indicative of their highly amorphous characters. The carbon contents of the studied samples are collected in Table S2. These values were used to correct the eventual electrode capacity.

TEM micrographs showed sub-micrometric agglomerations of particles in which two different domains can be discerned (Fig. 3). On the one hand, the NASICON phase features darker sharp-edged particles which are engulfed into lighter domains attributed to the carbon conductive phase. The sol–gel route here employed ensures this homo-
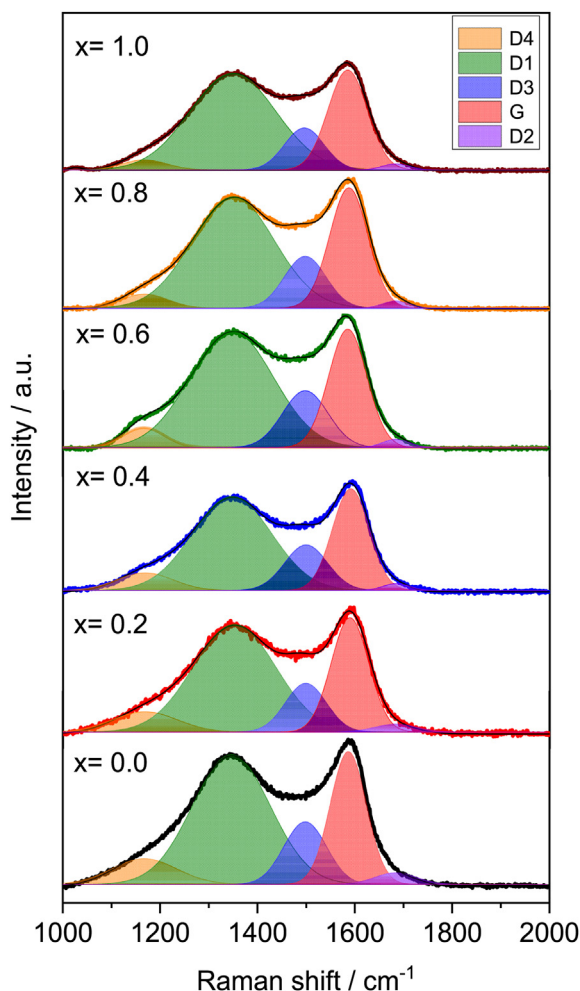

Fig. 2. a) Raman spectra of Na$_{4-x}$VFe$_x$Mn$_{1-x}$(PO$_4$)$_3$ (0 ≤ x ≤ 1) samples scanned with a green light laser (λ$_0$ = 532 nm). Deconvoluted bands have been filled with distinct colors to remark their contributions. (For interpretation of the references to color in this figure legend, the reader is referred to the web version of this article.)
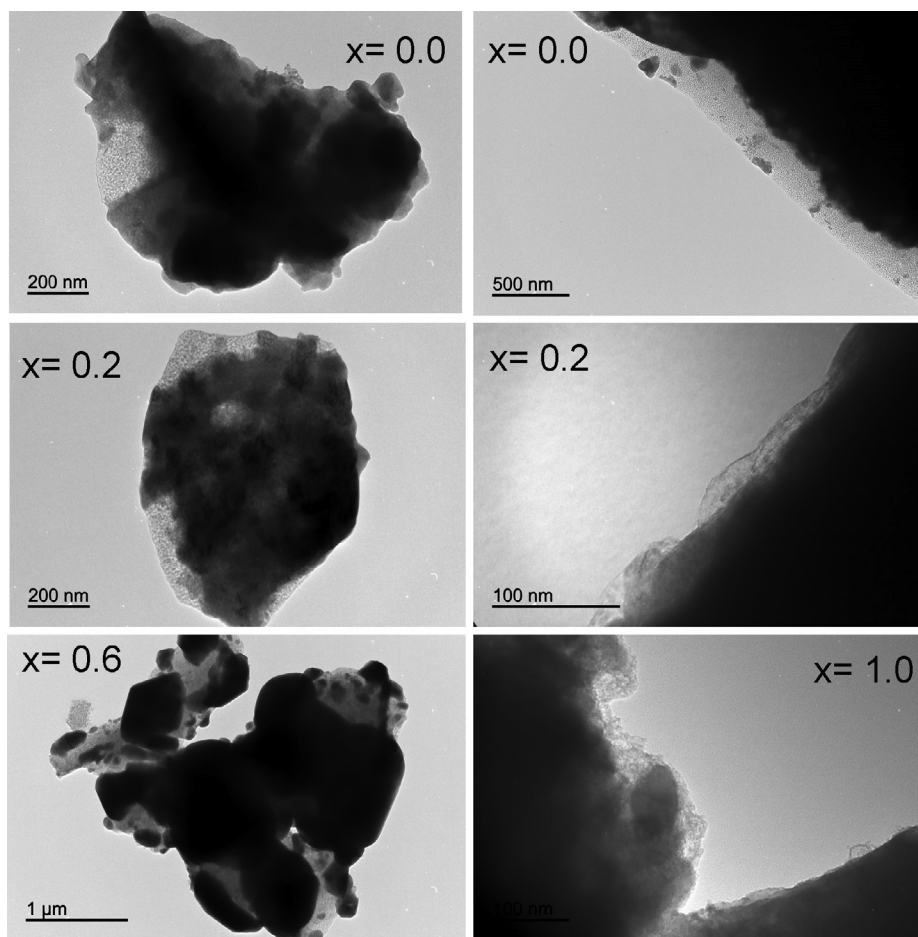
Fig. 3. Transmission electron images of selected $Na_{4-x}VFe_xMn_{1-x}(PO_4)_3$ ($0 \leq x \leq 1$) samples.

geneous distribution of both phases, which favorably contributes to facilitating the electrical conductivity among the electrochemically active particles of the electrode. In addition, the carbon coating may preserve the source of NASICON particles from corrosive reactions during the electrochemical reaction. The efficiency of the here employed sol–gel route to yield samples in which the compositing elements are homogeneously dispersed was confirmed by EDX analysis (Figure S1). Chemical composition was determined by this technique and XRF. The stoichiometric values are written in Table S3 and evidence a close similarity to the nominal ones.

Cyclic voltammograms of sodium half-cells revealed reversible profiles ascribable to faradic processes when cycled between 1.8 and 3.9 V (Fig. 4a). Two anodic bands appear at ca. 2.5 V and ca. 3.5 V with their corresponding cathodic counterparts. The contribution of the former signal progressively increases when the iron content is also augmented. For the samples with the highest iron content ($x \geq 0.8$), the cathodic band is split. This effect has been already reported by several authors in related compounds. Balaya et al. reported that local heating can be induced by high charge/discharge rates and subsequently structural rearrangements by the transfer of Na ions from the Na(1) to the Na(2) sites [34]. Otherwise, Zheng et al reported the appearance of this effect even at a rate as low as 0.2C. According to these authors, this feature can be ascribed to difficulties when trying to insert two Na^+ ions [35]. Although this effect is more clearly visible for those samples with the highest iron content, we cannot discard its presence in the lower intense signals of samples with $\times < 0.8$. Following the same assumption, the bands at ca. 3.5 V appears strongly split for the lowest iron contents $\times \leq 0.2$ and progressively merge when manganese is replaced by iron.

On increasing the iron content, both bands are progressively shifted to lower potentials. This linear tendency of the thermodynamic potentials has been plotted in Fig. 4b as the cell voltages at which the current peaks are positioned. It can be interpreted as evidence of a homogeneous distribution of both iron and manganese in the NASICON structures. The rigidity of the polyanionic structure involves that the shortening of the metal–oxygen bond lengths, which largely contribute to the cell contraction. Thus, the diminution of $M-O$ bond lengths, when Mn^{2+} is replaced by Fe^{3+}, involves a decrease of the ionic character of the transition metals. This situation can augment the V 3d–O 2p antibonding state leading to the lower cell potential [36]. A careful inspection of Fig. 4b allows determining a parallel tendency in both anodic and cathodic peaks for the high voltage signal. Contrarily, the cathodic band at ca. 2.5 V appears significantly polarized when the iron content is augmented. It could be correlated to signal splitting and the hindrances to Na^+ insertion. Fig. 5a shows the first charge and discharge cycle recorded at C10. The flat plateaus at ca. 3.5 V are commonly ascribed to the reversible redox reaction of V^{4+}/V^{3+} and Mn^{3+}/Mn^{2+} redox couples [28], while that of ca. 2.5 V is typically assigned to Fe^{3+}/Fe^{2+} one [37]. The length of the first discharge plateaus linearly varied according to the nominal stoichiometry of the studied samples (Fig. 5b), which confirms the validity of the assignation of these plateaus.

To assure the validity of this assumption, XPS spectra of fully charged and subsequently discharged electrodes were recorded for a selected sample with intermediate composition (x = 0.6). (Fig. 6). Spectra at the V2p core level showed the two broadened bands ascribed to $V2p_{3/2}$ (517.0 eV) and $V2p_{1/2}$ (523.5 eV) transitions. These values agree well with the occurrence of trivalent vanadium [38,39].

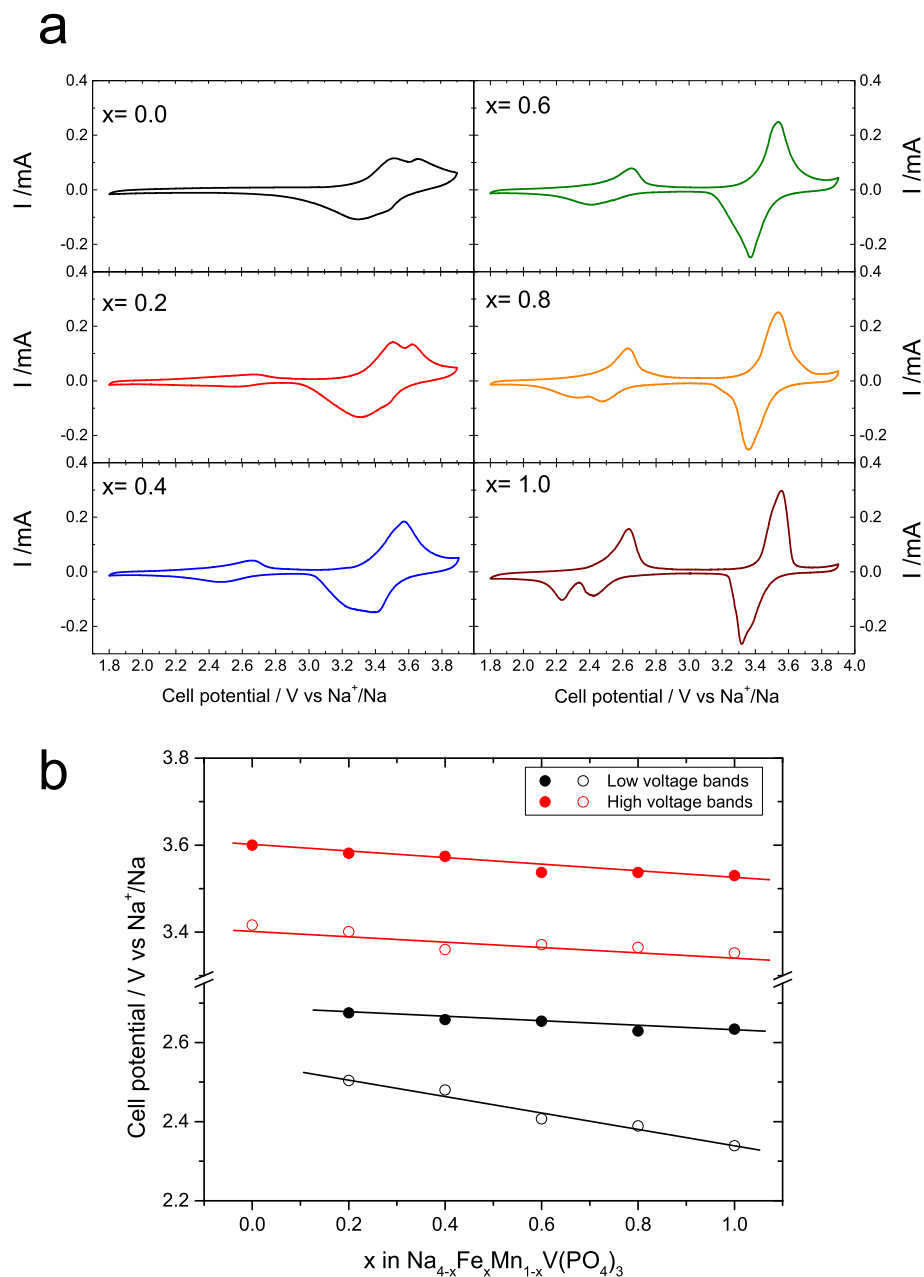**Fig. 4.** a) Cyclic voltammograms for $Na_{4-x}VFe_xMn_{1-x}(PO_4)_3$ samples recorded at a scan rate of 0.1 mV s^{-1}; b) Linear variations of cell potential at the current peaks versus composition.

The small band at ca. 520 eV is commonly attributed to an O1s satellite. Similarly, Mn2p$_{3/2}$ and Mn2p$_{1/2}$ transitions are revealed by signals at 641.4 eV and 653.2 eV, which evidence the presence of Mn^{2+} in the raw material [40]. Finally, Fe2p spectrum shows Fe2p$_{3/2}$ and Fe2p$_{1/2}$ bands corresponding to iron in trivalent state at 712.1 eV and 725.4 eV, respectively [41]. The Mn2p and V2p spectra recorded for the electrode charged at 3.9 V show a significant band shifting to higher binding energies, which agrees with the expected oxidation of these transition metals at the end of the plateau at 3.5 V. Otherwise, the Fe 2p bands remained unshifted after full discharge. Further discharge up to the lower cut-off voltage revealed a position retrieving for V2p and Mn2p spectra, while a new band at lower binding energies (710.5 eV) would justify the occurrence of reduced iron to the divalent state [41].

Structural changes induced by sodium extraction/insertion were examined by recording *ex-situ* XRD patterns on the later sample (x = 0.6) at several points of the first cycle (Fig. 7). Splitting of reflections indicating the occurrence of a two-phase system could be observed in neither charge nor discharge. The reflections shifted according to changes in the unit cell during Na$^+$ extraction/insertion. It was quantified by calculating the cell parameters, which are included in Table 1. The values evidence a slight cell contraction during the first charge. Parameter *a* monotonically decreased, while the value of c initially decreased to eventually reach values close to that of the raw material. This anisotropic variation was also reported for $Na_3VCr(PO_4)_3$ [42]. Further discharge involved a continuous increase of both crystallographic parameters. It was more abrupt for the last stage of discharge for which the reduction of Fe^{3+} is expected to occur.

The electrochemical performance of the studied samples was determined by subjecting sodium-half cells to cycling at increasing rates from C/10 to 5C and then retrieving the initially low rate for a few cycles (Fig. 8a). The discharge capacity for the first cycle ranged from
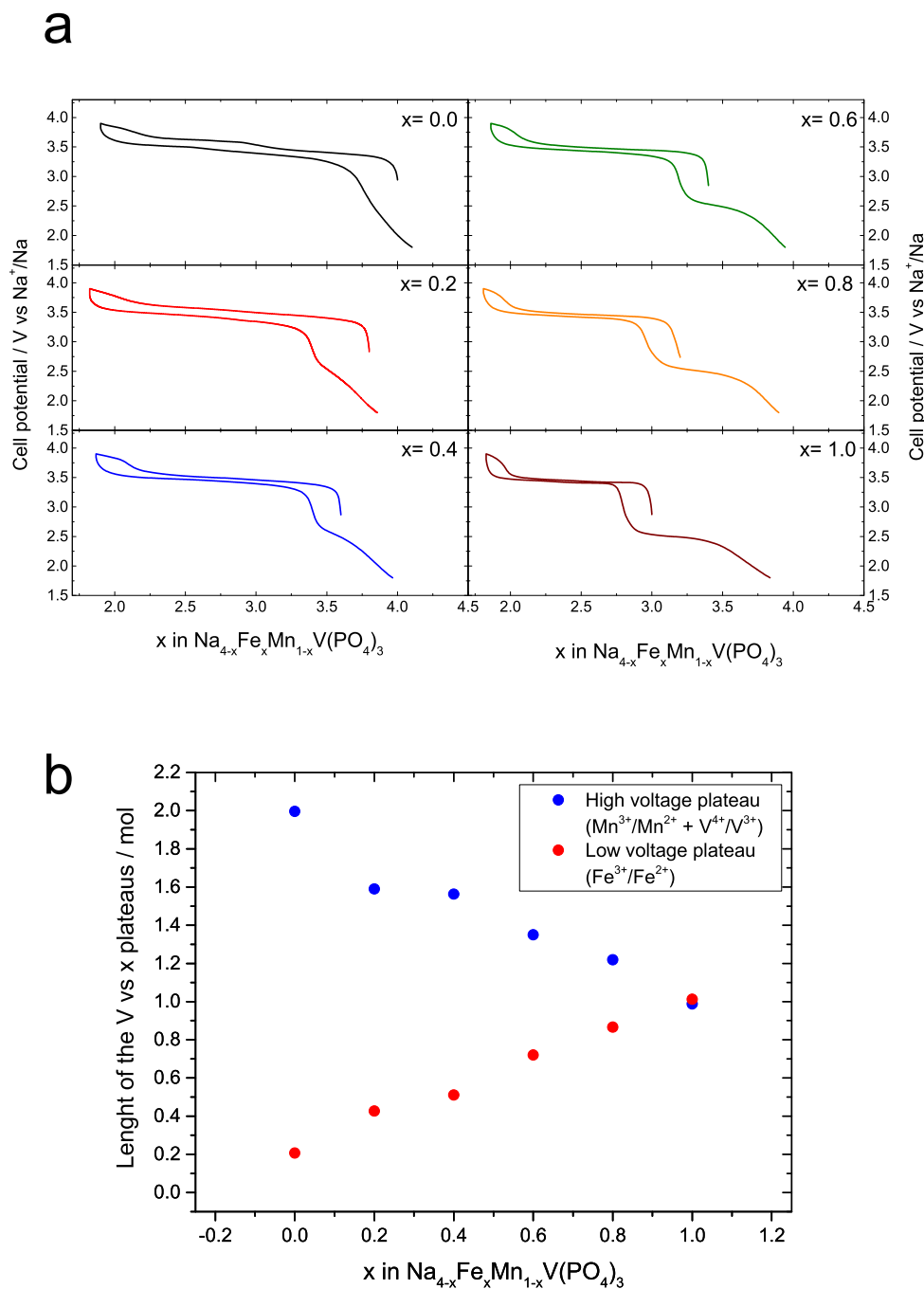
Fig. 5. a) First charge and discharge branches of sodium half-cells assembled with the studied samples. Rate: C/10; b) Linear relationships between the length of the high and low voltage plateaus and iron content in $Na_{4-x}VFe_xMn_{1-x}(PO_4)_3$ ($0 \leq x \leq 1$).

121 mA h g^{-1} for the sample with x = 0, which was close to the theoretical value calculated for this stoichiometry (125 mA h g^{-1}) to the lowest value of 102 mA h g^{-1} for the sample with the highest content of iron (x = 1.0). On increasing the rate, the effect of iron becomes more evident, providing better capacity retention. Thus, the Mn-free sample (x = 1.0) was able to sustain 85.5 mA h g^{-1}, while it decreased to 50.5 mA h g^{-1} for the sample with × = 0.4. At 5C, a clear correlation between discharge capacity and iron content is observed that, surprisingly, led to poor performance for samples with × ≤ 0.2. Likely, it should be related to the tendency of Mn-containing samples to suffer irreversible structural transformation occurring near to the upper cut-off voltage. It has been reported that charging at the region from 3.8 to 4.0 V leads to the extraction of Na$^+$ mainly from the Na1

position as evidenced by the enlargement of Na1 − O distance as compared to Na2 − O one. It is reflected by an irreversible structural evolution when cycling over 4.0 V during the first cycle. In our case, the upper cut-off voltage was limited to 3.9 V to avoid this undesirable effect, though the poor cyclability observed for samples with × ≤ 0.2, could be correlated to this effect [43,44].

On decreasing the rate to 0.1C after 30 cycles, iron-containing samples, particularly for x = 0.6, displayed good capacity recovery. Fig. 8b shows selected charge and discharge curves at the different cycling rates. On increasing the iron content, the plateaus ascribable to the faradic reactions become less steep, while the charge and discharge hysteresis decrease. It allows the sample with x = 0.1 to achieve high capacity values before reaching the cut-off voltages.
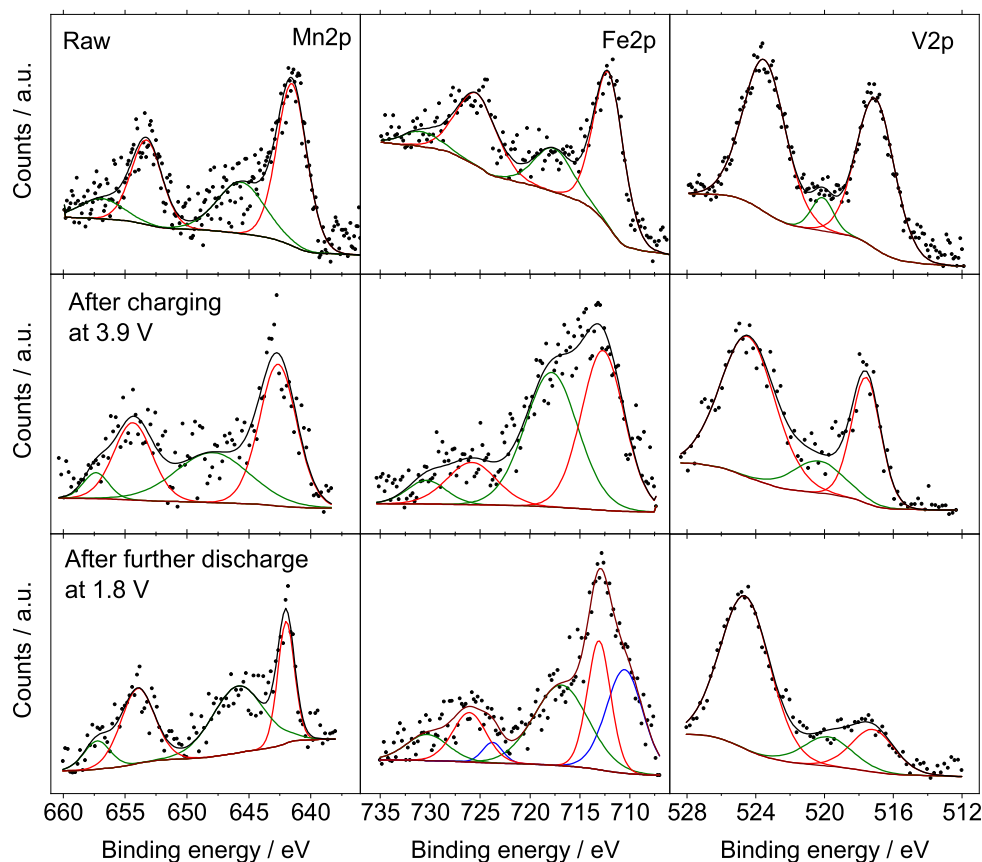
Fig. 6. X-ray photoelectron spectra at the Mn2p, Fe2p, and V2p core levels for raw $Na_{3.4}VFe_{0.6}Mn_{0.4}(PO_4)_3$ sample and fully charged and discharged electrodes.

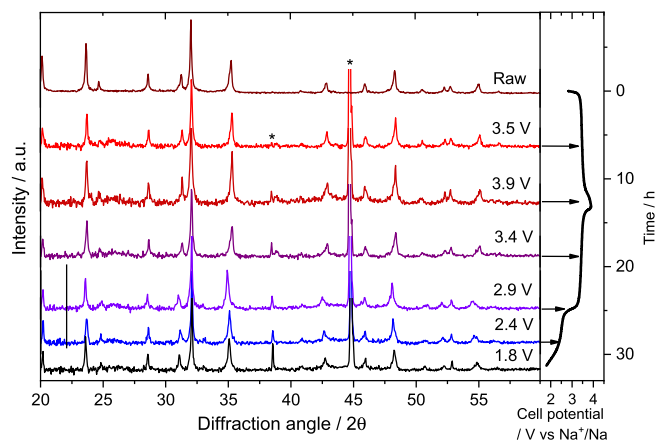**Fig. 7.** Ex-situ X-ray diffraction patterns of $Na_{3.4}VFe_{0.6}Mn_{0.4}(PO_4)_3$ recorded at several points of the first cycle. Reflections ascribable to the Al support are labeled with an asterisk.

Table 1
Calculated cell parameters in the R-$3c$ space group calculated from XRD patterns of $Na_{3.4}VFe_{0.6}Mn_{0.4}(PO_4)_3$ electrodes at different points of the first cycle.

	a / Å	c / Å	Volume /Å³
Raw	8.814(2)	21.654(5)	1456.5(7)
Charged at 3.5 V	8.795(4)	21.633(7)	1449(1)
Fully charged at 3.9 V	8.794(3)	21.662(5)	1451(1)
Discharged at 3.4 V	8.795(3)	21.653(6)	1450(1)
Discharged at 2.9 V	8.815(2)	21.787(5)	1466(1)
Discharged at 2.4 V	8.862(1)	21.818(8)	1484(1)
Fully discharged at 1.8 V	9.008(4)	21.821(9)	1533(2)

According to these results, samples with high iron contents were chosen to perform extended cycling at 1C (Fig. 8c). These experiments confirmed the beneficial effect of iron substitution on $Na_3V_2(PO_4)_3$, so that the capacity retention for the sample with x = 1.0 was 98% and 88% after 100 and 150 cycles, respectively. Otherwise, this value decreased to 72% for x = 0.8 after 150 cycles. Likely, the better electrochemical performance of samples containing high iron contents could be explained by the slight decrease of the operational voltage at the high voltage plateau. The occurrence of irreversible structural transformations over to 4 V has been reported for $Na_4VMn(PO_4)_3$ [45]. This fact has been demonstrated to be deleterious for the reversibility of the electrochemical reaction. Thus, shifting down the charge–discharge voltage of this plateau may positively contribute to preserving the NASICON framework to sustain cycling at high rates and for a large number of cycles.

To justify these results, the kinetic response of these electrode materials was determined by different techniques. In this way, Randles-Sevcik set a linear correlation between the maximum at the peak current of the faradic signals in cyclic voltammograms recorded at different scan rates and the square root of the scan rate, allowing to calculate the apparent chemical diffusion coefficients ($D_{Na^+}^{app}$) (Figure S1) [46]:

$$I_p = 2.69 \times 10^{-5} n^{3/2} S (D_{Na^+}^{app})^{1/2} C v^{1/2} \qquad (1)$$

In this equation, C refers to sodium concentration, S to the electrode geometric area, and n is the number of electrons transferred during the electrochemical reaction. Fig. 9a shows the linear relationship between I_p and $v^{1/2}$ so that the diffusion coefficients can be determined from the slope. For this purpose, high (peaks 2 and 3) and low (peaks 1 and 4) voltage signals were selected as indicated in Figure S2. Fig. 9b evidences a progressive increase of the coefficients with the iron con-
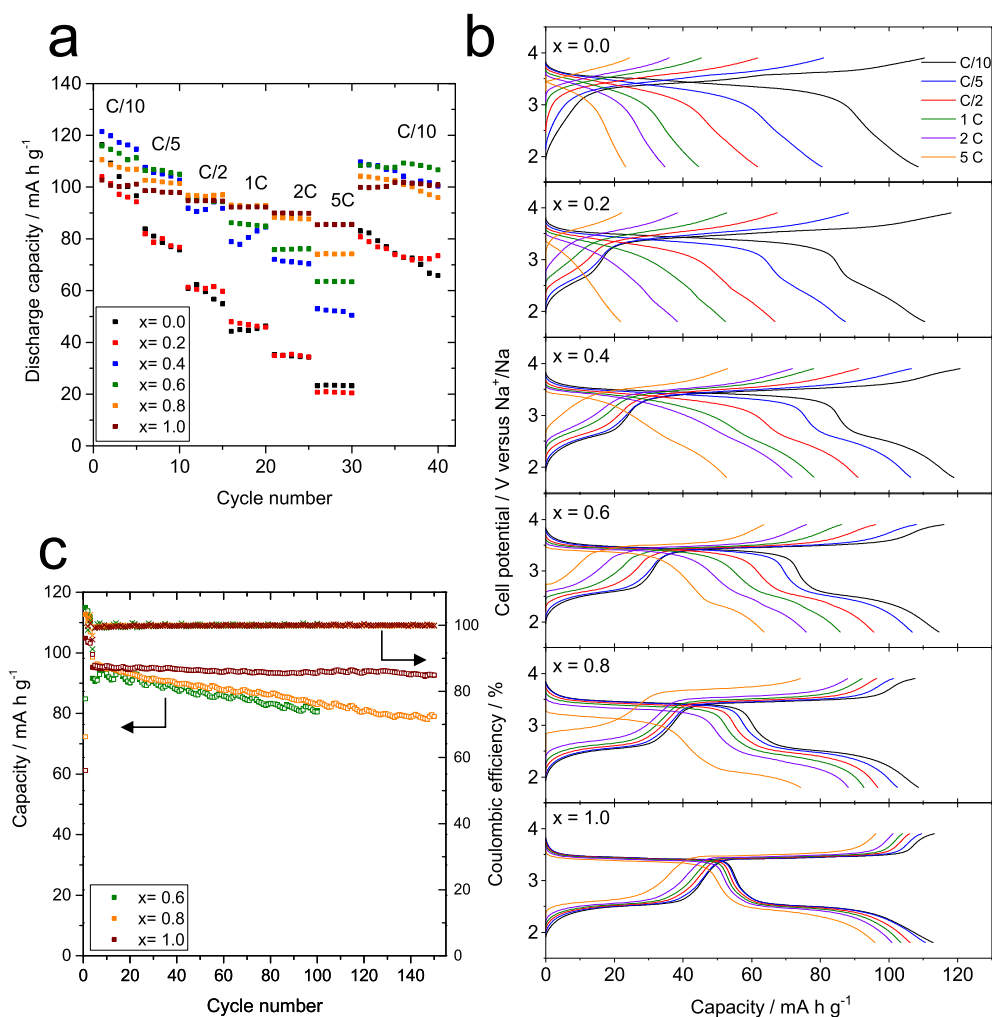
Fig. 8. a) Rate capability of sodium half-cells assembled with $Na_{4-x}VFe_xMn_{1-x}(PO_4)_3$ ($0 \leq x \leq 1$) samples and cycled at rates ranging from C/10 to 5C and then C/10; b) selected charge and discharge curves recorded at rates from C/10 to 5C; c) Extended galvanostatic cycling of samples with $\times \geq 0.6$ at 1C (closed symbols: discharge; open symbols: charge).

tent, though lower coefficients were determined for the signals corresponding to the Fe^{3+}/Fe^{2+} redox couple. It means that even if the Na^+ diffusion is slower during the participation of iron in the electrochemical reaction, the incorporation of iron to the NASICON structure involves an overall improvement of the kinetic response of the electrode material.

The determination of the internal cell resistance at the electrode–electrolyte interphase may also offer relevant information about the electrochemical behavior of the electrode material at an elevated kinetic regime. Fig. 10a-c shows the electrochemical impedance spectra, plotted as Nyquist diagrams, recorded on the end member of the series and a selected compound with intermediate composition ($x = 0.6$). They were recorded at several points of the first cycle at C/10 and after nine additional cycles at 1C. These profiles featured two overlapped semicircles at high and medium frequencies, typically ascribed to resistive and capacitive phenomena existing at the solid electrolyte interface deposited onto the surface layer and during the charge-transfer reaction occurring at the electrode surface. To elucidate the resistance values, the diagrams were fitted to the equivalent circuit included in Fig. 10d. In this scheme, R_{sl} and R_{ct} are respectively the resistance values at the surface layer and charge transfer reaction. The fitted spectra appear in the figure at lines overlapping the experimental spectra (symbols) to evidence the goodness of fitting. These resistance values are written in Table 2.

Along the first cycle, R_{sl} showed more constancy values than R_{ct}. More abrupt changes were observed for R_{ct} values, which were significantly higher before extracting sodium, at full charge and full discharge. It can be correlated to initial barriers to charge transfer when sodium is completely extracted from Na2 sites or fully inserted in available sites. In any case, resistance values were notoriously lower for the sample with $x = 1.0$. After running nine additional cycles at 1C, iron-containing samples preserved resistance values close to that of the first cycles, evidencing the stability of their NASICON structure on cycling. Otherwise, a large increase of the R_{ct} value was determined for the iron-free samples, which agrees to its poor behavior at high rates (Fig. 8a).

Impedance spectra can also be used for calculating apparent diffusion coefficients of sodium ions ($D_{Na^+}^{app}$) and comparing results with those obtained by cyclic voltammetry. The cell was allowed to relax for a few hours before measuring the spectra. Thus, these coefficients should reflect the diffusivity of sodium in a quasi-equilibrium state. To achieve this goal, the real impedance (Z') is plotted versus the reciprocal root square of the lower angular frequencies ($\omega^{-1/2}$) (Figure S3). From the slope of the linear segment, the Warburg impedance coefficient (σ_w) can be deduced from equation (2)[47]:

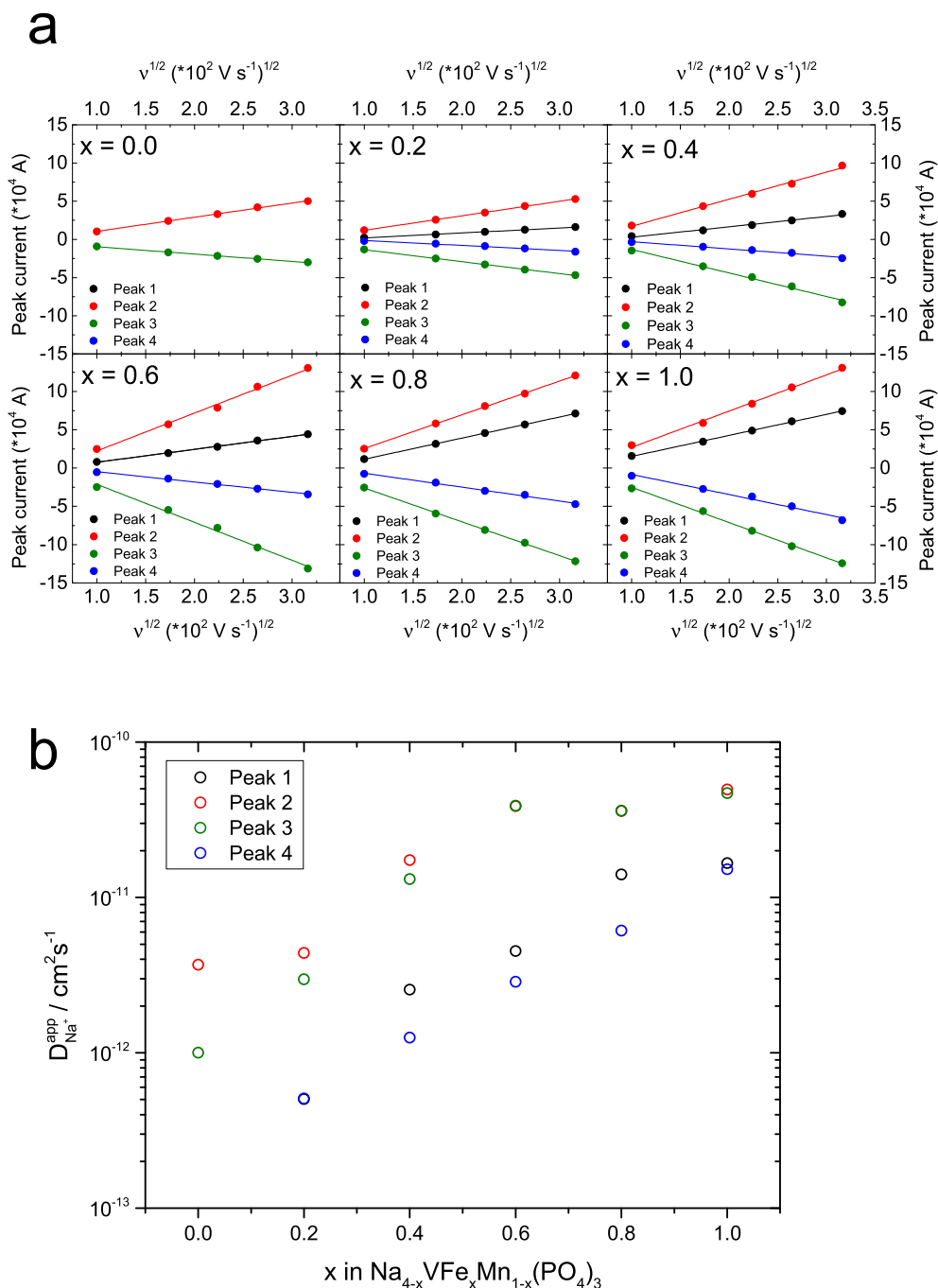$$Z' = R_{sl} + R_{ct} + \sigma_w \times \omega^{-1/2} \qquad (2)$$

Fig. 9. a) Plots of the peak current (I_p) versus the square root of the scan rate ($\nu^{1/2}$) and b) Plot of the apparent diffusion coefficients, calculated by Randles-Sevcik equation for $Na_{4-x}VFe_xMn_{1-x}(PO_4)_3$ ($0 \leq x \leq 1$) samples.

Then, the apparent diffusion coefficient ($D_{Na^+}^{app}$) can be determined from the next equation:

$$D_{Na^+}^{app} = \frac{1}{2}\left(\frac{RT}{SF^2\sigma_w C}\right)^2 \tag{3}$$

being R the gas constant expressed in $J\,K^{-1}\,mol^{-1}$, T is the absolute temperature, S the geometrical area of the electrode in cm^2, F the Faraday's constant, and C the molar concentration of Na^+ ions in $mol\,cm^{-3}$. The results in Table 2 revealed an increase of the diffusion coefficients, measured at the voltage plateaus, when the iron content is increased, which agrees with the results obtained from

voltammetry. Notwithstanding, the latter values we roughly one order lower than the former ones, which can be attributed to the inherent incertitude of the employed techniques.

4. Conclusion

Six samples with nominal $Na_{4-x}VFe_xMn_{1-x}(PO_4)_3$ ($0 \leq x \leq 1$) stoichiometry have been studied as positive electrodes for sodium-ion batteries. The citric-based sol–gel route yielded high purity phases in which the constituting elements appeared homogeneously dispersed on the particle surface, as determined by X-ray diffraction and electron
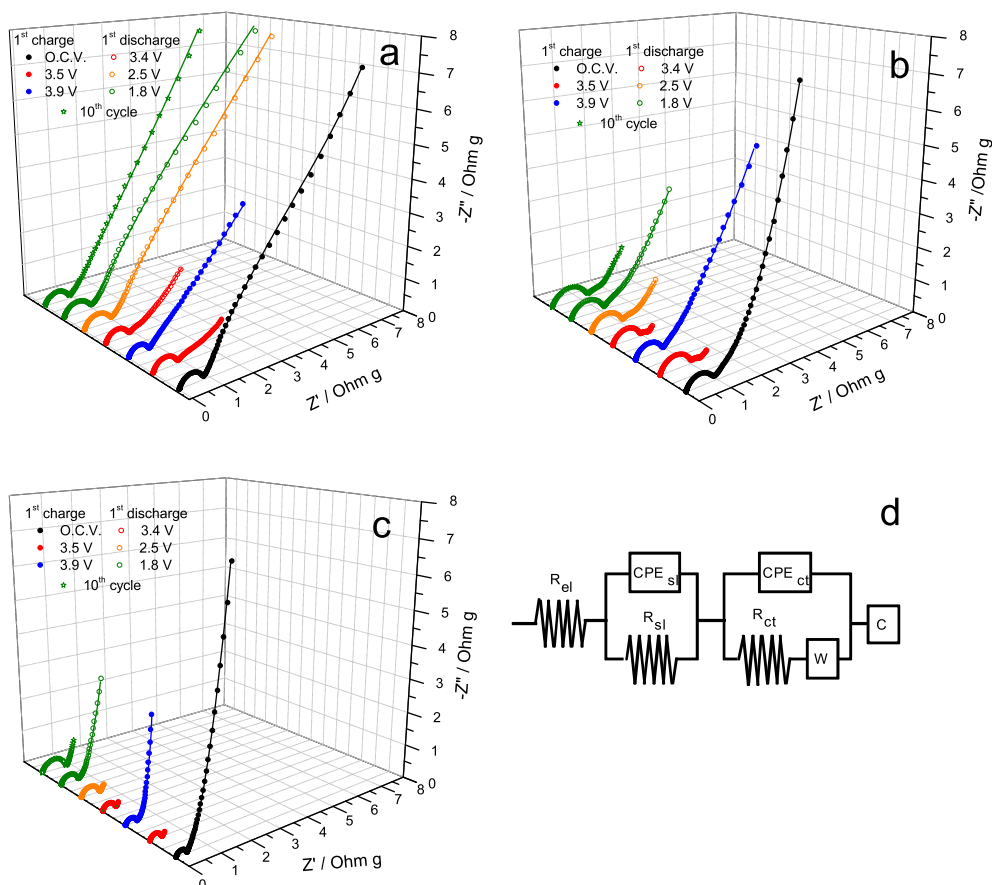
Fig. 10. Experimental and fitted Nyquist plots of $Na_{4-x}VFe_xMn_{1-x}(PO_4)_3$ ($0 \leq x \leq 1$) samples with x = a) x = 0.0, b) x = 0.6 and c) x = 1.0 at several points of the first cycle; d) Equivalent circuit used for the fitting of the spectra.

Table 2

Surface layer (R_{sl}) and charge transfer resistance (R_{ct}) values, Warburg coefficients (σ_W), and diffusion coefficients ($D_{Na^+}^{app}$) calculated from the impedance spectra recorded for samples with x = 0.0, 0.6 and 1.0 after one cycle at C/10 followed by nine additional cycles at 1C.

		R_{sl} / Ohm g	R_{ct} / Ohm g	σ_W / Ohm s$^{-1/2}$	$D_{Na^+}^{app}$ ./ cm^2 s^{-1}
x = 0.0	O.C.V.	0.77	10.82	189.34	3.46 10^{-15}
x = 0.6		0.91	0.81	106.42	1.43 10^{-14}
x = 1.0		0.33	0.79	34.70	1.68 10^{-13}
x = 0.0	Charge at 3.5 V	1.02	0.74	32.25	2.12 10^{-13}
x = 0.6		1.01	0.26	8.46	3.58 10^{-12}
x = 1.0		0.23	0.14	1.70	1.00 10^{-10}
x = 0.0	Full charge at 3.9 V	0.63	9.89	67.69	1.08 10^{-13}
x = 0.6		0.86	9.39	92.86	5.42 10^{-14}
x = 1.0		0.36	4.13	12.08	3.12 10^{-12}
x = 0.0	Discharge at 3.4 V	0.77	0.51	35.68	1.73 10^{-13}
x = 0.6		0.91	0.22	8.16	3.85 10^{-12}
x = 1.0		0.41	0.04	1.61	1.12 10^{-10}
x = 0.0	Discharge at 2.5 V	0.91	21.72	190.67	4.45 10^{-15}
x = 0.6		1.07	0.34	34.48	1.36 10^{-13}
x = 1.0		0.50	0.10	2.89	2.42 10^{-11}
x = 0.0	Full discharge at 1.8 V	0.93	18.89	200.13	3.09 10^{-15}
x = 0.6		1.15	0.35	74.46	2.11 10^{-14}
x = 1.0		0.58	0.09	17.12	3.88 10^{-13}
x = 0.0	After 10 cycles	0.83	71.84	108.59	1.05 10^{-14}
x = 0.6		1.24	0.44	31.87	1.15 10^{-13}
x = 1.0		0.74	0.09	6.98	2.33 10^{-12}

microscopy. A carbon conductive phase was in-situ generated because of the thermal decomposition of citric acid in the inert atmosphere. Raman spectra evidenced their low levels of graphitization.

Cyclic voltammograms featured two main reversible faradic signals at ca. 3.5 V and ca. 2.5 V respectively attributed to V^{4+}/V^{3+} and Mn^{3+}/Mn^{2+}, and Fe^{3+}/Fe^{2+} redox couples. These bands progressively shifted down to lower potentials when the iron content increased, which has been explained in terms of a shortening of the metal–oxygen bond when Mn^{2+} is replaced by the smaller Fe^{3+}. Moreover, galvanostatic tests evidenced that the length of these plateaus

matched well to the transition metal content existing in each sample. Ex-situ XPS spectra recorded in a selected raw sample with x = 0.6 confirmed the expected oxidation state of the transition metals. Also, it evidenced the oxidation of V and Mn after a full charge of the cell and further reduction at the lower cut-off voltage, remarking the occurrence of iron in the divalent state. Ex-situ-XRD patterns recorded during the first cycle did not reveal the appearance of a two-phase system. The change in cell parameters was more pronounced along the 2.5 V region in which Fe^{3+} is reduced.

The evaluation of the kinetic response of these electrode materials evidenced the better electrochemical behavior of the $Na_3VFe(PO_4)_3$ sample both at a high rate and long cycling. It was correlated to its high apparent diffusion coefficients calculated by voltammetric and impedance methods. Likely, the shifting down of the cell operational voltage preserves the NASICON framework from irreversible structural transformations and allows sustaining prolonged cycling at high rates.

CRediT authorship contribution statement

P. Lavela: Conceptualization, Formal analysis, Writing - Original Draft, Visualization. **R. Klee:** Investigation, Validation Data Curation. **M.A. Hidalgo:** Investigation, Validation Data Curation. **J.L. Tirado:** Funding acquisition, Supervision, Resources.

Declaration of Competing Interest

The authors declare that they have no known competing financial interests or personal relationships that could have appeared to influence the work reported in this paper.

Acknowledgments

Appendix A. Supplementary data

Supplementary data to this article can be found online at https://doi.org/10.1016/j.jelechem.2021.115533.

References

[1] T.C. Wanger, The lithium future-resources, recycling, and the environment, Conserv. Lett. 4 (2011) 202–206, https://doi.org/10.1111/j.1755-263X.2011.00166.x.

[2] A. Eftekhari, D.-W. Kim, Sodium-ion batteries: new opportunities beyond energy storage by lithium, J. Power Sources 395 (2018) 336–348, https://doi.org/10.1016/j.jpowsour.2018.05.089.

[3] X. Pu, H. Wang, D. Zhao, H. Yang, X. Ai, S. Cao, Z. Chen, Y. Cao, Recent progress in rechargeable sodium-ion batteries: toward high-power applications, Small 15 (32) (2019) 1805427, https://doi.org/10.1002/smll.v15.3210.1002/smll.201805427.

[4] A. Mauger, C.M. Julien, State-of-the-art electrode materials for sodium-ion batteries, Materials (Basel) 13 (2020) 3453, https://doi.org/10.3390/ma13163453.

[5] C. Vaalma, D. Buchholz, M. Weil, S. Passerini, A cost and resource analysis of sodium-ion batteries, Nat. Rev. Mater. 3 (2018) 18013, doi:10.1038/natrevmats.2018.13.

[6] S.H. Mohr, G.M. Mudd, D. Giurco, Lithium resources and production: critical assessment and global projections, Minerals 2 (2012) 65–84, https://doi.org/10.3390/min2010065.

[7] P.K. Nayak, L. Yang, W. Brehm, P. Adelhelm, From lithium-ion to sodium- ion batteries: advantages, challenges, and surprises, Angew. Chem. Int. Ed. 57 (1) (2018) 102–120, https://doi.org/10.1002/anie.201703772.

[8] M. Okoshi, Y. Yamada, A. Yamada, H. Nakai, Theoretical analysis on de-solvation of lithium, sodium, and magnesium cations to organic electrolyte solvents, J.

Electrochem. Soc. 160 (11) (2013) A2160–A2165, https://doi.org/10.1149/2.074311jes.

[9] H.S. Hirsh, Y. Li, D.H.S. Tan, M. Zhang, E. Zhao, Y.S. Meng, Sodium-ion batteries paving the way for grid energy storage, Adv. Energy Mater. 10 (32) (2020) 2001274, https://doi.org/10.1002/aenm.v10.3210.1002/aenm.202001274.

[10] V. Palomares, P. Serras, I. Villaluenga, K.B. Hueso, J. Carretero-Gonzalez, T. Rojo, Na-ion batteries, recent advances and present challenges to become low cost energy storage systems, Energy Environ. Sci. 5 (2012) 5884–5901, https://doi.org/10.1039/c2ee02781j.

[11] C. Delmas, J.J. Braconnier, C. Fouassier, P. Hagenmuller, Electrochemical inter-calaction of sodium in Na_xCoO_2 bronzes, Solid State Ion. 4 (1981) 165–169, https://doi.org/10.1016/0167- 2738(81)90076- X.

[12] Q. Liu, H.u. Zhe, M. Chen, C. Zou, H. Jin, S. Wang, Q. Gu, S. Chou, P2-type $Na_{2/3}Ni_{1/3}Mn_{2/3}O_2$ as cathode materials with high-rate and long-life for sodium ion storage, J. Mater. Chem. A 7 (2019) 9215–9221, https://doi.org/10.1039/C8TA11927A.

[13] S.-P. Guo, J.-C. Li, Q.-T. Xu, Z.e. Ma, H.-G. Xue, Recent achievements on polyanion-type compounds for sodium-ion batteries: Syntheses, crystal chemistry and electrochemical performance, J. Power Sources 361 361 (2017) 285–299, https://doi.org/10.1016/j.jpowsour.2017.07.002.

[14] L.N. Zhao, T. Zhang, H.L. Zhao, Y.L. Hou, Polyanion-type electrode materials for advanced sodium-ion batteries, Materials Today Nano 10 (2020) 100072, https://doi.org/10.1016/j.mtnano.2020.100072.

[15] K. Hurlbutt, S. Wheeler, I. Capone, M. Pasta, Prussian blue analogs as battery materials, Joule 2 (10) (2018) 1950–1960, https://doi.org/10.1016/j.joule.2018.07.017.

[16] Y. Uebou, T. Kiyabu, S. Okada, J.-I. Yamaki, electrochemical sodium insertion into the 3d framework of $Na_3M_2(PO_4)_3$ (M = Fe, V), The Rep. Inst. Adv. Mater. Study 16 (2002) 1–4, https://doi.org/10.15017/7951.

[17] L.S. Plashnitsa, E. Kobayashi, Y. Noguchi, S. Okada, J.-I. Yamaki, Performance of NASICON symmetric cell with ionic liquid electrolyte, J. Electrochem. Soc. 157 (2010) A536–A543, https://doi.org/10.1149/1.3298903.

[18] X. Zhang, X. Rui, D. Chen, H. Tan, D. Yang, S. Huang, Y. Yu, $Na_3V_2(PO_4)_3$: An advanced cathode for sodium-ion batteries, Nanoscale 11 (6) (2019) 2556–2576, https://doi.org/10.1039/C8NR09391A.

[19] I.V. Zatovsky, NASICON-type Na3V2(PO4)3. Acta Cryst. E66 (2010) i12. doi:10.1107/S1600536810002801.

[20] M. Chen, Q. Liu, Z. Hu, Y. Zhang, G. Xing, Y. Tang, S.-L. Chou, Designing advanced vanadium-based materials to achieve electrochemically active multielectron reactions in sodium/potassium-ion batteries, Adv. Energy Mater. 10 (42) (2020) 2002244, https://doi.org/10.1002/aenm.v10.4210.1002/aenm.202002244.

[21] Y. Chen, J. Cheng, Y. Wang, C. Wang, Z. He, D. Li, L.i. Guo, Insights into the elevated electrochemical performance and kinetic characteristics of magnesium-substituted $Na_3V_{2-x}Mg_x(PO_4)_3/C$ with superior rate capability and long lifespan, J. Mater. Sci. 55 (27) (2020) 13141–13156, https://doi.org/10.1007/s10853-020-04962-3.

[22] M.J. Aragón, P. Lavela, G.F. Ortiz, J.L. Tirado, Effect of iron substitution in the electrochemical performance of $Na_3V_2(PO_4)_3$ as cathode for Na-ion batteries, J. Electrochem. Soc. 162 (2) (2015) A3077–A3083, https://doi.org/10.1149/2.0151502jes.

[23] R. Klee, P. Lavela, M. Aragón, R. Alcántara, J.L. Tirado, Enhanced high-rate performance of manganese substituted $Na_3V_2(PO_4)_3/C$ as cathode for sodium-ion batteries, J. Power Sources 313 (2016) 73–80, https://doi.org/10.1016/j.jpowsour.2016.02. 066.

[24] Y. Chen, J. Cheng, C. Wang, Y. Wang, D. Li, L. Guo, Simultaneous modified Na2.9V1.9Zr0.1(PO4)3/C@rGO as a superior high rate and ultralong lifespan cathode for symmetric sodium ion batteries, Chem. Eng. J. 413 (2021) 127451, doi: 10.1016/j.cej.2020.127451.

[25] X. Ma, X. Cao, Y. Zhou, S. Guo, X. Shi, G. Fang, A. Pan, B. Lu, J. Zhou, S. Liang, Tuning crystal structure and redox potential of NASICON-type cathodes for sodium-ion batteries, Nano Res. 13 (12) (2020) 3330–3337, https://doi.org/10.1007/s12274-020-3011-6.

[26] X. Wang, S. Roy, Q. Shi, Y. Li, Y. Zhao, J. Zhang, Progress and Application Prospects in Advanced and Cost-effective Iron (Fe)-based Cathode Materials for Sodium-ion Batteries, J. Mater. Chem. A 9 (2021) 1938–1969, https://doi.org/10.1039/D0TA10610K.

[27] M. Chen, Q. Liu, S.-W. Wang, E. Wang, X. Guo, S.-L. Chou, High-abundance and low-cost metal-based cathode materials for sodium-ion batteries: problems, progress, and key technologies, Adv. Energy Mater. 9 (14) (2019) 1803609, https://doi.org/10.1002/aenm.v9.1410.1002/aenm.201803609.

[28] W. Zhou, L. Xue, X. Lu, H. Gao, Y. Li, S. Xin, G. Fu, Z. Cui, Y. Zhu, J.B. Good-enough, NaxMV(PO4)3 (M = Mn, Fe, Ni) structure and properties for sodium extraction, Nano Lett. 16 (2016) 7836, doi: 10.1021/acs.nanolett.6b04044 .

[29] B.M. de Boisse, J. Ming, S.-I. Nishimura, A. Yamada, alkaline excess strategy to NASICON-type compounds towards higher-capacity battery electrodes, J. Electrochem. Soc. 163 (7) (2016) A1469–A1473, https://doi.org/10.1149/2.0041608jes.

[30] R. Klee, P. Lavela, J.L. Tirado, Effect of the Mn/V ratio to optimize the kinetic properties of $Na_{3+x}Mn_xV_{1-x}Cr(PO_4)_3$ positive electrode for sodium-ion batteries, Electrochim. Acta 375 (2021) 137982, https://doi.org/10.1016/j.electacta.2021.137982.

[31] P. Lavela, R. Klee, J.L. Tirado, On the benefits of Cr substitution on $Na_4MnV(PO_4)_3$ to improve the high voltage performance as cathode for sodium-ion batteries, J. Power Sources 495 (2021) 229811, https://doi.org/10.1016/j.jpowsour.2021.229811.

[32] F. Tuinstra, J.L. Koenig, Raman spectrum of graphite, J. Chem. Phys. 53 (3) (1970) 1126–1130, https://doi.org/10.1063/1.1674108.

[33] A. Sadezky, H. Muckenhuber, H. Grothe, R. Niessner, U. Pöschl, Raman microspectroscopy of soot and related carbonaceous materials: Spectral analysis and structural information, Carbon 43 (8) (2005) 1731–1742, https://doi.org/10.1016/j.carbon.2005.02.018.

[34] K. Saravanan, C.W. Mason, A. Rudola, K.H. Wong, P. Balaya, The first report on excellent cycling stability and superior rate capability of $Na_3V_2(PO_4)_3$ for sodium ion batteries, Adv. Energy Mater. 3 (4) (2013) 444–450, https://doi.org/10.1002/aenm.v3.410.1002/aenm.201200803.

[35] L.-L. Zheng, Y. Xue, B.-S. Liu, Y.-X. Zhou, S.-E. Hao, Z.-b. Wang, High performance $Na_3V_2(PO_4)_3$ cathode prepared by a facile solution evaporation method for sodium-ion batteries, Ceram. Int. 43 (6) (2017) 4950–4956, https://doi.org/10.1016/j.ceramint.2016.12.149.

[36] G. Kobayashi, A. Yamada, S.-I. Nishimura, R. Kanno, Y.o. Kobayashi, S. Seki, Y. Ohno, H. Miyashiro, Shift of redox potential and kinetics in $Li_x(Mn_yFe_{1-y})PO_4$, J. Power Sources 189 (1) (2009) 397–401, https://doi.org/10.1016/j.jpowsour.2008.07.085.

[37] M.J. Aragón, C. Vidal-Abarca, P. Lavela, J.L. Tirado, High reversible sodium insertion into iron substituted $Na_{1+x}Ti_{2-x}Fe_x(PO_4)_3$, J. Power Sources 252 (2014) 208–213, https://doi.org/10.1016/j.jpowsour.2013.12.006.

[38] J. Li, J. Cheng, Y. Chen, C. Wang, L.i. Guo, Effect of K/Zr co-doping on the elevated electrochemical performance of $Na_3V_2(PO_4)_3$/C cathode material for sodium ion batteries, Ionics 27 (1) (2021) 181–190, https://doi.org/10.1007/s11581-020-03791-3.

[39] H. Wang, Y. Li, C. Huang, Y. Zhong, S. Liu, High-rate capability of $Li_3V_2(PO_4)_3$ /C composites prepared via a polyvinylpyrrolidone-assisted sol–gel method, J. Power Sources 208 (2012) 282–287, https://doi.org/10.1016/j.jpowsour.2012.02.055.

[40] U. Nisar, R.A. Shakoor, R. Essehli, R. Amin, B. Orayech, Z. Ahmad, P.R. Kumar, R. Kahraman, S. Al-Qaradawi, A. Soliman, Sodium intercalation/de- intercalation mechanism in $Na_4MnV(PO_4)_3$ cathode materials, Electrochim. Acta 292 (2018) 98–106, https://doi.org/10.1016/j.electacta.2018.09.111.

[41] R. Dedryvère, M. Maccario, L. Croguennec, F. Le Cras, C. Delmas, D. Gonbeau, X-Ray photoelectron spectroscopy investigations of carbon-coated Li_xFePO_4 materials, Chem. Mater. 20 (22) (2008) 7164–7170, https://doi.org/10.1021/cm801995p.

[42] R. Liu, G. Xu, Q.i. Li, S. Zheng, G. Zheng, Z. Gong, Y. Li, E. Kruskop, R. Fu, Z. Chen, K. Amine, Y. Yang, Exploring highly reversible 1.5-electron reactions ($V^{3+}/V^{4+}/V^{5+}$) in $Na_3VCr(PO_4)_3$ cathode for sodium-ion batteries, ACS Appl, Mater. Interfaces 9 9 (50) (2017) 43632–43639, https://doi.org/10.1021/acsami.7b1301810.1021/acsami.7b13018.s001.

[43] M.V. Zakharkin, O.A. Drozhzhin, I.V. Tereshchenko, D. Chernyshov, A.M. Abakumov, E.V. Antipov, K.J. Stevenson, Enhancing Na^+ extraction limit through high voltage activation of the NASICON-type $Na_4MnV(PO_4)_3$ cathode, ACS Appl. Energy Mater. 1 (11) (2018) 5842–5846, https://doi.org/10.1021/acsaem.8b0126910.1021/acsaem.8b01269.s001.

[44] F. Chen, V.M. Kovrugin, R. David, O. Mentré, F. Fauth, J.-N. Chotard, C. Masquelier, A NASICON-type positive electrode for Na batteries with high energy density: $Na_4MnV(PO_4)_3$, Small Methods 3 (4) (2019) 1800218, https://doi.org/10.1002/smtd.v3.410.1002/smtd.201800218.

[45] M.V. Zakharkin, O.A. Drozhzhin, S.V. Ryazantsev, D. Chernyshov, M.A. Kirsanova, I.V. Mikheev, E.M. Pazhetnov, E.V. Antipov, K.J. Stevenson, Electrochemical properties and evolution of the phase transformation behavior in the NASICON type $Na_{3-x}Mn_xV_{2-x}(PO_4)_3$ ($0 \leq x \leq 1$) cathodes for Na-ion batteries, J. Power Sources 470 (2020) 228231, https://doi.org/10.1016/j.jpowsour.2020.228231.

[46] T. Jiang, W. Pan, J. Wang, X. Bie, F. Du, Y. Wei, C. Wang, G. Chen, Carbon coated $Li_3V_2(PO_4)_3$ cathode material prepared by a PVA assisted sol–gel method, Electrochim. Acta 55 (12) (2010) 3864–3869, https://doi.org/10.1016/j.electacta.2010.02.026.

[47] A.Y. Shenouda, H.K. Liu, Preparation, characterization, and electrochemical performance of Li_2CuSnO_4 and $Li_2CuSnSiO_6$ electrodes for lithium batteries, J. Electrochem. Soc. 157 (2010) A1183–A1187, https://doi.org/10.1149/1.3479425.